Inorganic Chemistry

Article

pubs.acs.org/IC

Magnetic Structures of $LiMBO_3$ (M = Mn, Fe, Co) Lithiated Transition Metal Borates

Liang Tao,[†] James R. Neilson,[‡,⊥] Brent C. Melot,[§] Tyrel M. McQueen,[‡] Christian Masquelier,[†] and Gwenaëlle Rousse*[,∥]

[†]Laboratoire de Réactivité et de Chimie du Solide (LRCS), CNRS UMR7314, Université de Picardie Jules Verne, 33 rue Saint Leu, 80039 Amiens, France

[‡]Department of Chemistry and Department of Physics and Astronomy, The Johns Hopkins University, 3400 N. Charles Street, Baltimore, Maryland 21218, United States

[§]Department of Chemistry, University of Southern California, 3620 McClintock Avenue, Los Angeles, California 90089-1062, United States

[∥]Institut de Minéralogie et de Physique des Milieux Condensés (IMPMC), UMR 7590 CNRS−Université Pierre et Marie Curie UPMC Université de Paris 06, 4 Place Jussieu, 75252 Paris Cedex 05, France

Supporting Information

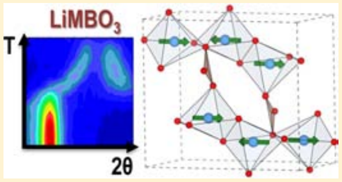

ABSTRACT: The magnetic ordering within $LiMBO_3$ compounds (M = Mn, Fe, and Co) has been explored by magnetization measurements and neutron powder diffraction. For all M, an incommensurately ordered magnetic phase is established on cooling, followed by a change to a commensurate long-range antiferromagnetic state below T_{N2} = 12(1) K for $LiMnBO_3$, T_{N2} = 25(1) K for $LiFeBO_3$, and T_{N2} = 12(1) K for $LiCoBO_3$. For $LiMnBO_3$, the magnetic ordering at T = 2 K exhibits a propagation vector $\mathbf{k}$ = (1, 0, 0) and consists of antiferromagnetic chains that are coupled antiferromagnetically to each other, the magnetic moments being oriented along the [001] direction. In contrast, the magnetic order at T = 2 K in $LiFeBO_3$ and $LiCoBO_3$ exhibits a propagation vector of $\mathbf{k}$ = ($^1/_2$, $^1/_2$, $^1/_2$) and consists of ferromagnetic chains that are antiferromagnetically coupled. The magnetic moments lie roughly along the $[02\bar{3}]$ direction within the *bc* plane for $LiFeBO_3$, and along the $[30\bar{1}]$ direction within the *ac* plane for $LiCoBO_3$. The moment orientations in both $LiMnBO_3$ and $LiFeBO_3$ suggest an Ising character arising from unquenched orbital momentum due to unusual trigonal bipyrimidal coordination environments. No evidence of Ising behavior is found in the case of $LiCoBO_3$.

1. INTRODUCTION

Li-ion batteries are widely used in our daily life, from personal electronic devices to automotive vehicles. The discovery and development of olivine-type $LiFePO_4$[1,2] as cathode materials for such devices paved the way for many alternative compositions and structural families like silicates,[3−5] borates,[6,7] and fluorosulfates[8−10] of transition metal elements. The knowledge of the magnetic structures of electrode materials is of importance for two reasons: it can reveal interesting physics which may otherwise go unnoticed, and it is a prerequisite for *accurate* density functional theory (DFT) calculations or prediction of new materials for energy storage. Such studies have been extensively reported for several polyanionic compounds with most of the attention on phosphates[11−14] and sulfates.[15,16]

Yet, it was not until 2001 when Legagneur et al.[6] first reported the successful preparation of $LiMBO_3$ (M = Mn, Fe, Co) that transition metal borates drew attention from the battery community, due to the high theoretical capacity of $LiFeBO_3$ (220 mA h g^{-1}, i.e., 30% higher than $LiFePO_4$). $LiMBO_3$ (M = Mn, Fe, Co) compounds crystallize in the monoclinic space group $C2/c$.[6,7,17−22] Note that these phases are distinct from the hexagonal ($P\bar{6}$) polymorph of $LiMnBO_3$ which we will not discuss here.[6] The structure is composed of edge-sharing MO_5 trigonal bipyramids which are bound together *via* BO_3 planar triangles to form a polyanionic framework. Compounds with magnetic interactions with reduced dimensionality can yield fascinating magnetic ground states such as quantum spin liquids in $LiCuSbO_4$[23] or magneto-dielectric phenomena as in $CoSeO_4$.[24] Furthermore, the detailed nuclear structure of $LiFeBO_3$ is extremely complex,[22,25] though no detailed studies have yet employed powder neutron diffraction to obtain contrast to the lighter elements. In this Article, we report on a detailed analysis of the neutron powder diffraction patterns and magnetic susceptibility for the family of $LiMBO_3$ compositions (M = Mn, Fe, Co), and provide strong indications to the reduced dimensionality and unusual trigonal bipyramidal local coordination geometry of the transition metal ions within these compounds. More broadly, our results demonstrate the importance of being able to prepare compounds in unique coordination environments to produce novel electronic and magnetic phenomena.[26,27]

2. EXPERIMENTAL DETAILS

2.1. Synthesis. Isotopically substituted compounds $^7LiM^{11}BO_3$ (M = Mn, Fe, Co) were prepared through traditional ceramic routes as described elsewhere:[25] iron(II) oxalate dihydrate ($FeC_2O_4{\cdot}2H_2O$, 99% Alfa Aesar)/cobalt(II) hydroxide ($Co(OH)_2$, Umicore 99%)/Mn(II) oxalate

Received: July 1, 2013
Published: October 2, 2013

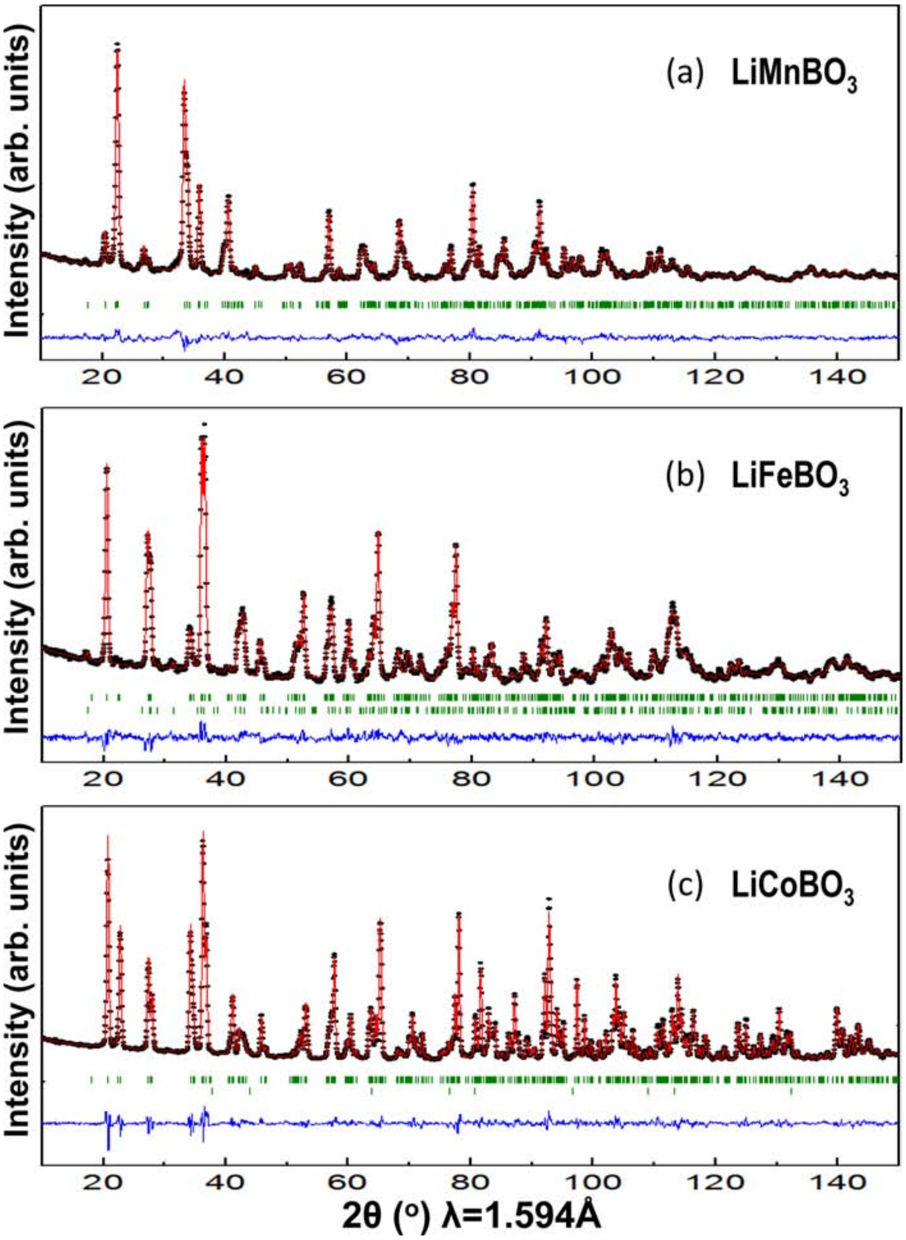

Figure 1. Rietveld refinement of $LiMBO_3$ (M = Mn, Fe, Co) neutron patterns (collected on D2B at ILL, λ = 1.594 Å) for (a) monoclinic $LiMnBO_3$, $\chi^2 = 3.55$, $R_{Bragg} = 5.35\%$, $R_f = 3.52\%$, $R_p = 2.58\%$, $R_{wp} = 3.30\%$; (b) $LiFeBO_3$, $\chi^2 = 6.15$, $R_{Bragg} = 5.38\%$, $R_f = 3.11\%$, $R_p = 3.45\%$, $R_{wp} = 4.40\%$, a minor impurity $LiBO_2$ is added as secondary phase; (c) $LiCoBO_3$, $\chi^2 = 4.90$, $R_{Bragg} = 3.50\%$, $R_f = 2.34\%$, $R_p = 3.17\%$, $R_{wp} = 4.14\%$, a minor impurity CoO is added as secondary phase. Black dots correspond to experimental data, the red line is the calculated fit, and the blue line is the difference between calculation and observed patterns. The vertical green marks represent the Bragg peaks' positions.

dihydrate ($MnC_2O_4{\cdot}2H_2O$, Umicore 99%), boric acid ($H_3{}^{11}BO_3$, 99% Aldrich), and lithium hydroxide monohydrate ($^{7}LiOH{\cdot}H_2O$, 99% Aldrich) were ball milled in acetone and dried prior to heating to 300 °C under a flow of Ar for 4 h. The resulting powder was subsequently pressed into 13 mm pellets and heated from 300 to 700 °C for 10 h under Ar. The sintered pellets were then immediately placed in an Ar-filled glovebox, and ground into a powder before further characterization.

2.2. Structural Characterization. The purities of the samples were checked by laboratory X-ray powder diffraction, with a Bruker D8 diffractometer equipped with Cu Kα radiation (λ_1 = 1.540 56 Å, λ_2 = 1.544 39 Å) and a LynxEye detector. Room temperature neutron powder diffraction data were acquired on isotopically enriched ^{11}B and ^{7}Li powders sealed under Ar in an 8 mm diameter vanadium tube, on the high-resolution diffractometer D2B of the Institute Laue Langevin (ILL, Grenoble, France) with a wavelength of 1.594 Å. Low temperature neutron powder diffraction patterns suitable for solving the magnetic structure were obtained using the high-intensity diffractometer D20 at ILL with an incident wavelength of 2.410 Å. The nuclear and magnetic structures were refined using the Rietveld method[28] as implemented in the FullProf program.[29] For the magnetic structure determination, Bertaut symmetry analyses[30] were carried out with the BasIReps program of the same suite of software. The structures were drawn and examined with the help of the FullProf Studio program as well as the Diamond visualization program.

2.3. Susceptibility Measurements. The temperature dependences of the magnetization of the $LiMBO_3$ compounds were measured at T = 2−300 K on powders immobilized and sealed in eicosane ($C_{20}H_{42}$) wax in polycarbonate capsules (loaded in an argon filled glovebox) to prevent oxidation of the powders from humidity. Measurements were performed using the ACMS option on a Physical Properties Measurement System (Quantum Designs, Inc.) in dc linear extraction mode. The samples were first cooled under zero-field, then

Table 1. Crystallographic Data and Global Agreement Factors of $LiMBO_3$ (M = Mn, Fe, Co) Derived from Rietveld Refinements on Room Temperature Neutron Powder Diffraction Patterns (λ = 1.594 Å D2B ILL Grenoble France)

	atom	SOF	*x*	*y*	*z*	B_{iso} (Å^2)	BVS
			M = Mn[a]				
$LiMnBO_3$	Li1	0.46(3)	0.662(5)	0.507(2)	0.173(5)	0.76(26)	1.03(3)
*C*2/*c*	Li2	0.54(3)	0.658(3)	0.512(3)	0.111(6)	0.76(26)	0.99(4)
a = 5.1985(1) Å	Mn	1.0	0.165(2)	0.338(1)	0.1248(7)	0.72(8)	1.95(2)
b = 8.9734(2) Å	B	1.0	0.1655(8)	0.6707(5)	0.1236(4)	0.17(5)	2.94(2)
c = 10.3638(3) Å	O1	1.0	0.4089(7)	0.1587(5)	0.0892(3)	0.53(7)	2.00(2)
β = 91.821(2)°	O2	1.0	0.7712(7)	0.3087(4)	0.1583(4)	0.55(8)	1.92(2)
V = 483.21(2) Å^3	O3	1.0	0.3188(9)	0.5474(4)	0.1266(5)	1.30(8)	1.93(3)
			M = Fe[b]				
$LiFeBO_3$	Li1	0.50(3)	0.667(4)	0.510(4)	0.170(3)	0.59(23)	1.02(4)
*C*2/*c*	Li2	0.50(3)	0.705(5)	0.480(3)	0.086(3)	0.59(23)	1.03(4)
a = 5.1614(1) Å	Fe	1.0	0.1613(9)	0.3329(6)	0.1235(4)	anisotropic	1.98(2)
b = 8.9080(2) Å	B	1.0	0.165(1)	0.6662(7)	0.1246(5)	0.55(5)	2.88(4)
c = 10.1643(3) Å	O1	1.0	0.405(1)	0.1638(7)	0.0879(5)	0.46(7)	2.00(3)
β = 91.225(2)°	O2	1.0	0.779(1)	0.3042(6)	0.1607(6)	0.89(9)	1.98(3)
V = 467.22(2) Å^3	O3	1.0	0.3158(1)	0.5404(4)	0.1261(7)	1.42(8)	1.90(3)
			M = Co[c]				
$LiCoBO_3$	Li1	0.52(1)	0.660(4)	0.510(1)	0.166(1)	0.44(9)	1.05(2)
*C*2/*c*	Li2	0.48(1)	0.672(2)	0.500(1)	0.091(1)	0.44(9)	1.02(2)
a = 5.1349(1) Å	Co	1.0	0.1593(9)	0.3337(7)	0.1247(6)	0.74(6)	1.85(1)
b = 8.8537(1) Å	B	1.0	0.1665(4)	0.6683(2)	0.1248(2)	0.30(3)	2.94(1)
c = 10.1079(1) Å	O1	1.0	0.4032(3)	0.1637(3)	0.0907(2)	0.64(3)	1.94(1)
β = 91.382(1)°	O2	1.0	0.7816(3)	0.3058(2)	0.1578(2)	0.51(4)	1.93(1)
V = 459.40(1) Å^3	O3	1.0	0.3087(4)	0.5389(2)	0.1262(3)	0.89(4)	1.97(1)

Anisotropic Thermal Parameters (Å^2) × 10^{-4}[d]

atom	U11	U22	U33	U12	U13	U23
Fe	186(14)	11(10)	234(14)	−9(16)	−162(9)	−2(18)

[a] R_{Bragg} = 5.35%, R_f = 3.52%, R_p = 2.58%, R_{wp} = 3.30%, χ^2 = 3.55. [b] R_{Bragg} = 5.38%, R_f = 3.11%, R_p = 3.45%, R_{wp} = 4.40%, χ^2 = 6.15. [c] R_{Bragg} = 3.50%, R_f = 2.34%, R_p = 3.17%, R_{wp} = 4.14%, χ^2 = 4.90. [d] The form of the anisotropic thermal parameters is $\exp[-2\pi^2(h^2a^{*2}U_{11} + k^2b^{*2}U_{22} + l^2c^{*2}U_{33} + 2hka^*b^*U_{12} + 2hla^*c^*U_{13} + 2klb^*c^*U_{23})]$.

the magnetization was measured on warming in a field of μ_0H = 1 T, and the field-cooled magnetization was measured on cooling. The magnetic susceptibility was approximated as $\chi \approx M/H$.

3. RESULTS

3.1. Crystal Structures of $LiMBO_3$ (M = Fe, Co, Mn).

The crystal structures of $LiMBO_3$ were redetermined from neutron powder diffraction at room temperature in order to better localize the low X-ray scattering power Li, B, and O atoms. To make this possible, we prepared ^{11}B- and ^7Li-enriched $LiMBO_3$ (M = Mn, Fe, Co) since natural boron, and to a lesser extent lithium, has high thermal neutron absorption cross sections. Rietveld refinements against high resolution neutron powder diffraction data (D2B) at *T* = 300 K were carried out starting from the published structural model. All three compounds could be perfectly described in the monoclinic space group *C*2/*c*. Small amounts of known impurities [3.3(2) wt % $LiBO_2$ for $LiFeBO_3$ and 0.8(3) wt % CoO for $LiCoBO_3$] were detected and included as secondary phases in the Rietveld refinements. Contrary to previous reports, difference Fourier maps indicate the presence of two crystallographically distinct lithium positions, which may result from the different preparatory routes or from the higher sensitivity to ^7Li positions using neutrons. The resulting Rietveld fits are shown in Figure 1, and structural parameters are given in Table 1. We include a bond valence sum analysis calculated using the Zachariasen formula

$$V_i = \sum_j s_{ij} = \sum_j e^{\frac{(d_0-d_{ij})}{0.37}}$$

with the parameter d_0, which characterizes a typical cation−anion distance, taken from Brown et al.[31] The obtained values reflect the expected formal valences, Li^+, M^{2+}, B^{3+}, and O^{2-}. We did not find any direct evidence for long-range order of the recently reported modulated structure of $LiFeBO_3$.[22] Short-range modulated regions, however, may be the origin of the split Li site necessary to describe the NPD data.

The crystal structures of $LiMBO_3$ (M = Fe, Co, Mn), illustrated in Figure 2, are built up from chains composed of edge-sharing $[MO_5]$ trigonal bipyramids running along $[\bar{1}01]$ that stack perpendicular to the [010] direction. These ribbons are connected through planar BO_3 triangles, and Li ions sit in tetrahedral coordination. Structurally speaking, the three $LiMBO_3$ (M = Mn, Fe, Co) compounds differ only by the size of the trigonal bipyramid in which the transition metal sits, with the triangular BO_3 units being rigid. This is reflected in the lattice parameters and unit cell volumes that continuously decrease when Mn^{2+} (ionic radius r_V = 0.75 Å) is replaced by Fe^{2+} (r_V = 0.71 Å) and Co^{2+} (r_V = 0.67 Å). On heating above 500−550 °C, monoclinic $LiMnBO_3$ transforms into an hexagonal polymorph, which crystallizes in the space group $P\bar{6}$. The magnetic structure of the latter was studied a decade ago[32] and was shown to be driven by the triangular frustration present in the structure and in the square pyramid coordination adopted by manganese atoms. Mn atoms in monoclinic $LiMnBO_3$ are also surrounded by five oxygen atoms, but the local symmetry is different (trigonal bipyramid). This unusual crystalline arrangement for M atoms can lead to peculiar

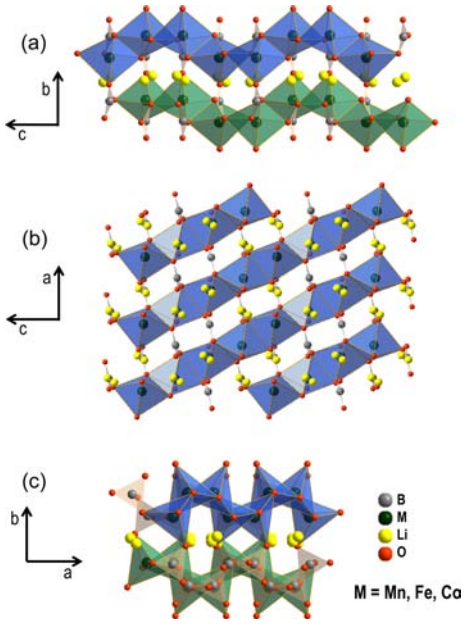

Figure 2. Monoclinic $LiMBO_3$ (M = Mn, Fe, Co) crystal structure along the *a*-axis (a), *b*-axis (b), and *c*-axis (c) to illustrate the connectivity of edge-sharing MO_5 trigonal bipyramids and BO_3 triangular units (boron is shown in gray, transition metal in dark green, lithium in yellow, and oxygen in red). In parts a and c, adjacent edge-shared MO_5 chains are colored in green and blue for clarity.

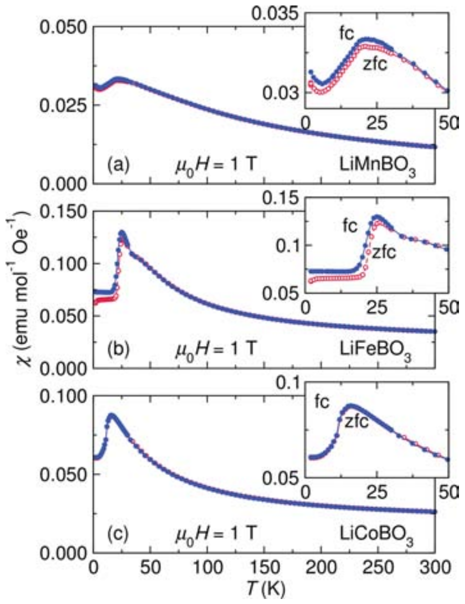

Figure 3. Temperature-dependent (2−300 K) magnetic susceptibility measurements collected in an external magnetic field of $\mu_0H = 1$ T for $LiMnBO_3$ (a), $LiFeBO_3$ (b), and $LiCoBO_3$ (c). The insets illustrate the cusps observed near T_{N1}, divergence at T_{N2}, as well as the small splitting between the zero-field cooled (zfc) and field-cooled (fc) measurements.

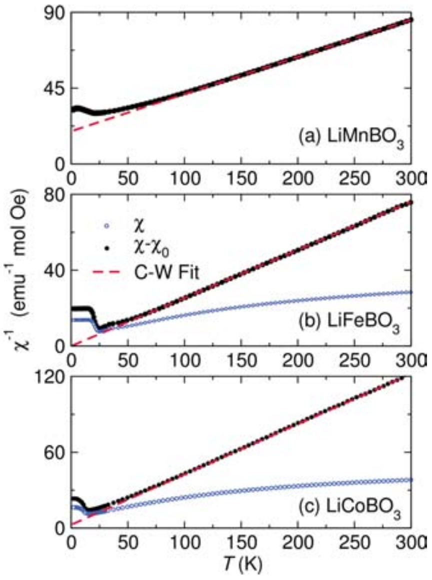

Figure 4. Temperature dependence of the inverse magnetic susceptibility (blue and black circles) and the fits to the Curie−Weiss equation (dashed red line) for $LiMnBO_3$ (a), $LiFeBO_3$ (b), and $LiCoBO_3$ (c). Subtraction of the temperature-independent susceptibility (χ_0) before inversion linearizes the data (black circles) between 150 K < T < 300 K for $LiFeBO_3$ and $LiCoBO_3$.

magnetic properties that we studied by means of magnetic susceptibility measurements and neutron powder diffraction.

3.2. Magnetic Susceptibility of $LiMBO_3$ (M = Mn, Fe, Co). The temperature-dependent magnetic susceptibility of all three compounds indicates Curie−Weiss behavior at high temperature ($T > 150$ K), and strong deviations thereof below $T = 50$ K, suggestive of antiferromagnetic order. Illustrated in Figure 3, the susceptibility for $LiMnBO_3$ and $LiCoBO_3$ shows no hysteresis between the zero-field-cooling (ZFC) and field-cooling (FC) measurements. However, $LiFeBO_3$ shows a splitting of the two measurements, which is often associated with the formation of magnetic domains with uncompensated moments (i.e., ferromagnetic or ferrimagnetic behavior) or spin-glass behavior. The susceptibility of $LiMnBO_3$ exhibits a cusp near $T \sim 23$ K, and $LiCoBO_3$ near $T \sim 16$ K. In the measurement of $LiFeBO_3$, however, a small upturn in the susceptibility near $T \sim 34$ K was observed and a maximum $T \sim 24$ K, followed by decrease to a plateau near $T \sim 18$ K, suggesting the presence of multiple ordering transitions.

Curie−Weiss analysis of the susceptibility measured from the three compounds provides insight to the distinct single-ion electronic configurations of the transition metals in the trigonal bipyramidal coordination environments. Paramagnetic spins follow a temperature dependence described by the Curie−Weiss equation

$$\chi = \frac{C}{T - \Theta_{cw}} + \chi_0 \tag{1}$$

where the Curie constant, C, is a metric of the moment coming from the spin and orbital contributions, Θ_{cw} is a metric of the mean-field interaction strength, and χ_0 is the temperature-independent contribution which may often arise from conduction electrons, core diamagnetism, or trace amounts of ferromagnetic impurities (e.g., Fe or Co). The linear inverse susceptibility, $1/\chi$, for $LiMnBO_3$ is indicative of paramagnetic Curie−Weiss behavior with $\chi_0 = 0$ (Figure 4). A linear fit to $(\chi - \chi_0)^{-1} = T/C - \Theta_{cw}/C$ (where $\chi_0 = 0$) from 150 K < T < 300 K allowed the determination of the effective moment ($\mu_{eff} = (8C)^{1/2}$), which is $\mu_{eff} = 6.02(1)$ μ_B. This value closely matches the predicted value for an $S = {}^5/_2$ ground state of a high-spin d^5 electronic configuration, $\mu_{calc} = 5.92$, as illustrated in the crystal field scheme of Figure 5. Furthermore, the data start to deviate from linearity below $T \sim 88$ K, which follows the mean field interaction strength determined from $\Theta_{cw} = -88.1(3)$ K.

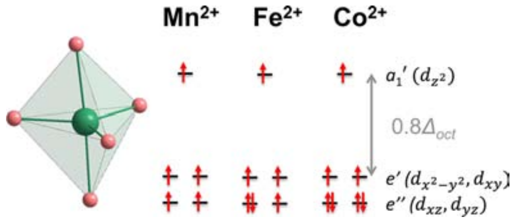

Figure 5. Proposed splitting and filling of the trigonal bipyramidal crystal fields (e″e′a$_1$′), as deduced from the effective moment in the Curie−Weiss fits of Figure 4, are schematically illustrated, scaled with respect to the splitting of an octahedral crystal field.

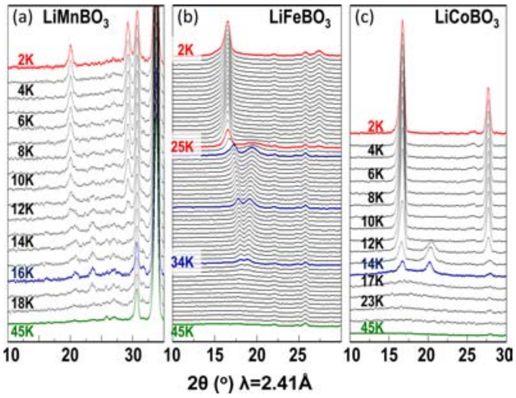

Figure 6. Neutron diffraction patterns (λ = 2.41 Å) as a function of temperature for (a) LiMnBO$_3$, (b) LiFeBO$_3$, and (c) LiCoBO$_3$. Prior to reaching the final antiferromagnetic ground state (LiMnBO$_3$ $T_{N2} \sim$ 12(1) K, LiFeBO$_3$ $T_{N2} \sim$ 25(1) K, and LiCoBO$_3$ $T_{N2} \sim$ 12(1) K), all three compounds go through an intermediate incommensurate phase as deduced from the shift of magnetic peaks with temperature.

Table 2. Magnetic Transition Domain of LiMBO$_3$ (M = Mn, Fe, Co) Determined from the Temperature Evolution of Magnetic Peaks of the Neutron Powder Diffraction Patterns Collected on D20, ILL

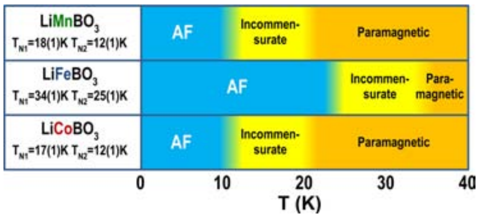

The inverse susceptibility of both LiFeBO$_3$ and LiCoBO$_3$ are nonlinear for χ_0 = 0; therefore, the quantity $(\chi - \chi_0)^{-1}$ was plotted for different values of χ_0 until the high-temperature region becomes linear and the corresponding fit to $(T - \Theta_{CW})/C$ over a temperature range of 150 K $< T <$ 300 K led to μ_{eff} = 5.62(1) μ_B for LiFeBO$_3$. From the free Fe^{2+} ion, one expects μ_{calc} = 4.90 μ_B in the case of complete quenching of the orbital momentum; however, in the case of an unquenched orbital moment that is decoupled from the spin, $(L + S)$, one expects μ_{calc} = 5.48 μ_B, whereas Russell−Saunders coupling predicts the total orbital angular momentum, $J = L + S$, to be μ_{calc} = 6.70 μ_B. Therefore, we infer that Fe^{2+} in LiFeBO$_3$ has a partially unquenched orbital moment. This is supported by the high-spin d^6 configuration of a trigonal bipyramidal crystal field (e″^{3}e′^{2}a$_1$′^{1}) depicted in Figure 5 that describes an effective orbital doublet, ^{5}E″. The value for Θ_{cw} = 0.3(3) K, together with the existence of magnetic order at low temperatures, implies that there is a combination of both ferromagnetic (positive valued) and antiferromagnetic (negative valued) interactions as a mean-field average. For LiCoBO$_3$, the effective moment μ_{eff} = 4.51(1) μ_B (Figure 4) is higher than the expected μ_{calc} = 3.87 μ_B for $S = {}^3/_2$ (fully quenched orbital momentum) and suggests some mixing of states at elevated temperatures, which could arise from the small energy splitting between the e′ and e″ manifolds. The value, Θ_{cw} = −6.6(3) K, also suggests a combination of both ferromagnetic and antiferromagnetic interactions for LiCoBO$_3$.

3.3. Magnetic Structure of LiMBO$_3$ (M = Mn, Fe, Co).

3.3.1. Incommensurate, Intermediate Magnetic Order. Neutron powder diffraction patterns recorded from room temperature to 2 K indicate the absence of any structural phase transition on cooling, with the lattice parameters showing a continuous evolution as a function of temperature (shown in Supporting Information). More interestingly, the neutron patterns reveal the existence of two successive transitions for each compound (Figure 6), with appearance of magnetic peaks indicative of a long-range ordering between the magnetic moments. Table 2 gathers the transition temperatures, T_{N1} and T_{N2}, for each compound.

In the intermediate temperature range ($T_{N1} > T > T_{N2}$), two magnetic peaks in the (16−25°) 2θ range emerge from a single broad feature of diffuse scattering located at 2θ ≈ 19°. The position of each peak shifts with temperature, akin to the incommensurate magnetic ordering of α-NaFeO$_2$.[33] For LiCoBO$_3$ at 13 K, the two magnetic peaks at 17.1° and 20.7° can be indexed with the propagation vector **k** = (0.47, 0.12, 0.15). For LiFeBO$_3$, the incommensurate magnetic peaks can be indexed with similar **k**-vectors: **k** = (0.47, 0.11, 0.09) at 25 K and **k** = (0.49, 0.11, 0.06) at 30 K. The low intensity of the principal magnetic peaks for LiMnBO$_3$ (21.3° and 24.0°) prevented us from obtaining a reliable propagation vector, but comparison of the patterns suggests it is similar to that found for the Fe and Co analogues.

Magnetic structures with incommensurate propagation vectors usually lead to sinusoidal or helical magnetic structures. Only two magnetic reflections are observed, precluding identifying a unique structural solution. Nonetheless, since the shortest magnetic propagation vector component lies along the chain direction (c^*), and the longest magnetic propagation vector components lie along the interchain directions (a^* or a^*b^*), it is likely that a sinusoidal or helical magnetic structure develops along the chain, with a reasonable degree of interaction between chains, as observed in compounds such as Li$_2$CuO$_2$[34] or NaCu$_2$O$_2$,[35] and LiCuVO$_4$.[36] As the temperature decreases, we speculate that the changes in the magnetic propagation vector reflects the evolution from a modulated magnetic structure along the chain direction into a collinear ordered ground state presenting a special **k**-vector inside or at the surface of the Brillouin zone that forms on cooling below T_{N2}. Such incommensurate-to-commensurate transitions are common in magnetic systems with competing interactions (e.g., α-NaFeO$_2$[33]).

3.3.2. Low-Temperature Magnetic Structure of LiMnBO$_3$. The magnetic reflections for LiMnBO$_3$ at T = 2 K can be indexed with a propagation vector **k** = (1, 0, 0), indicating that the magnetic unit cell is contained within the nuclear unit cell. The different possibilities of magnetic configurations were investigated using Bertaut's method[30] which allows determining the symmetry constraints between magnetic moments of atoms belonging to whatever crystallographic site. As mentioned previously, all the transition metal atoms of $LiMBO_3$ occupy trigonal bipyramids sites, corresponding to the Wyckoff position 8*f* of the space group *C*2/*c*. The atomic positions are labeled Mn2($\bar{x}$, y, $\bar{z} + {}^1/_2$), Mn3($\bar{x}$, $\bar{y}$, $\bar{z}$), and Mn4($\bar{x}$, $\bar{y}$, $z + {}^1/_2$) in relation to Mn1(x, y, z) by symmetry operations, with the four others being deduced by the C lattice centering (${}^1/_2$+, ${}^1/_2$+, 0).

The little group, G_k, coincides with the full $G = C2/c$ space group, as all the operators of G leave the propagation vector $\mathbf{k} = (1, 0, 0)$ invariant. The total magnetic representation Γ of the propagation vector group ($\mathbf{G_k} = C2/c$), for Wyckoff position 8*f*, can be decomposed on 4 irreducible representations of dimension 1 as follows

$$\Gamma(8f) = 3\Gamma_1 + 3\Gamma_2 + 3\Gamma_3 + 3\Gamma_4$$

which leads to 4 possible spin configurations, described by the basis functions

$$\begin{aligned}
\Gamma_1:\ & G^X = S_1^X - S_2^X + S_3^X - S_4^X \\
& F^Y = S_1^Y + S_2^Y + S_3^Y + S_4^Y \\
& G^Z = S_1^Z - S_2^Z + S_3^Z - S_4^Z \\
\Gamma_2:\ & A^X = S_1^X - S_2^X - S_3^X + S_4^X \\
& F^Y = S_1^Y + S_2^Y + S_3^Y + S_4^Y \\
& A^Z = S_1^Z - S_2^Z - S_3^Z + S_4^Z \\
\Gamma_3:\ & F^X = S_1^X + S_2^X + S_3^X + S_4^X \\
& G^Y = S_1^Y - S_2^Y + S_3^Y - S_4^Y \\
& F^Z = S_1^Z + S_2^Z + S_3^Z + S_4^Z \\
\Gamma_4:\ & C^X = S_1^X + S_2^X - S_3^X - S_4^X \\
& A^Y = S_1^Y - S_2^Y - S_3^Y + S_4^Y \\
& C^Z = S_1^Z + S_2^Z - S_3^Z - S_4^Z
\end{aligned}$$

Here, S_i^X, for instance, is the component along x of the magnetic moment of atom i. The x, y, and z axes are taken to point along the **a**, **b**, and **c** crystallographic axes. For example, Γ_1 corresponds to a *G*-type (+, −, +, −) antiferromagnetic coupling of the Mn atoms of the cell in the **x** and **z** directions, while in the **y** direction the moments are coupled ferromagnetically in sequence (+, +, +, +). We tried all the magnetic models by Rietveld refinements of the neutron diffraction data of $LiMnBO_3$ recorded at 2 K. Over all the possibilities determined by the symmetry analysis, the collinear solution $G^Z = S_1^Z - S_2^Z + S_3^Z - S_4^Z$ (corresponding to Γ_1) gives the best agreement between observed and calculated patterns (R_{mag} = 11.1%) (Figures 7a and 9a, resulting structure given in Table 3). This structure consists of antiferromagnetic chains that are coupled antiferromagnetically to each other, with the magnetic moment on each Mn^{2+} directed along the *c*-axis. The refined value of the magnetic moment, 3.31(4) μ_B, is lower than that expected for a high-spin electronic configuration for Mn^{2+} ($3d^5$ $e''^2 e'^2 a_1'^1$) inferred from the high temperature Curie−Weiss analysis. This discrepancy is likely due to either incomplete long-range ordering of the magnetic structure or the formation of a intermediate-spin Mn^{2+}ground state ($3d^5$: $e''^3 e'^2 a_1'^0, {}^4E''$). The fact that the moments lie along a particular crystal-field axis suggests an Ising character and unquenched orbital momentum, which would only be possible if the Mn^{2+} is low or intermediate spin, but further work is required to resolve this ambiguity.

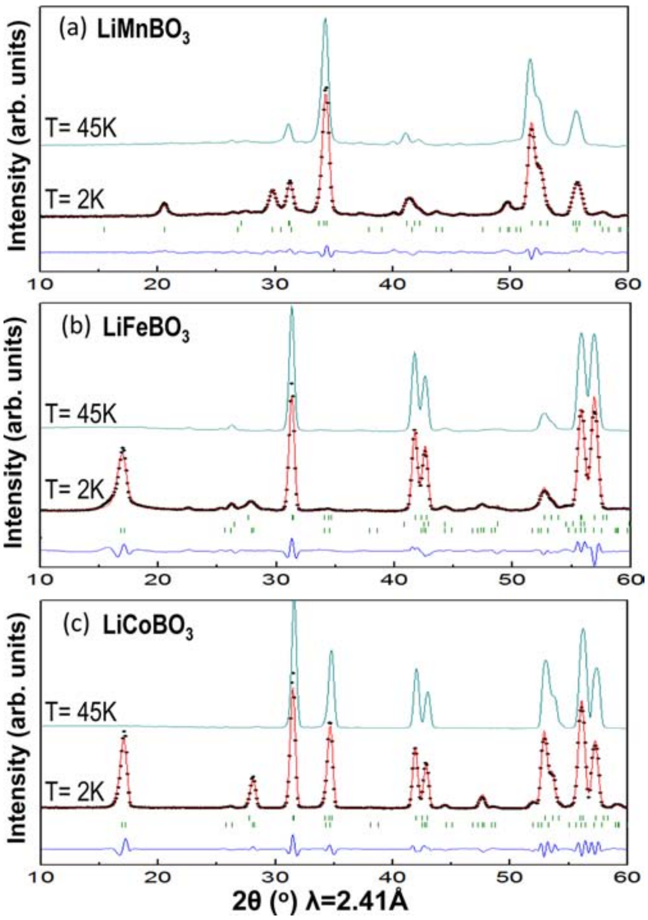

Figure 7. Rietveld refinement of $LiMBO_3$ diffraction patterns at 2 K (λ = 2.41 Å) corresponding to the ground state magnetic structure determination. In parts a, b, and c, the neutron diffraction data at 45 K (nuclear structure only) is shown as an upper cyan line. Black dots (observed), red line (calculated), green vertical marks (Bragg positions: 1st row, nuclear; 2nd row, magnetic), and blue line (difference between observed and calculation) are presented from top to bottom. For $LiFeBO_3$, the middle row of green bars represents a minor impurity $LiBO_2$, in addition to the nuclear (first row) and magnetic contributions (last row).

Table 3. Magnetic Structures of $LiMBO_3$ (M = Mn, Fe, Co) Determined from Neutron Powder Diffraction Data Collected on D20 at 2 K (λ = 2.41 Å, ILL Grenoble France)

atom	m_a (μ_B)	m_b (μ_B)	m_c (μ_B)	M_{total} (μ_B)
$LiMnBO_3$ $\mathbf{k}$ = (1, 0, 0)				
Mn1 (0.1650, 0.3380, 0.1248)	0	0	3.31(4)	3.31(4)
Mn2 (0.8350, 0.3380, 0.3752)	0	0	−3.31(4)	−3.31(4)
Mn3 (0.8350, 0.6620, 0.8752)	0	0	3.31(4)	3.31(4)
Mn4 (0.1656, 0.6620, 0.6248)	0	0	−3.31(4)	−3.31(4)
$LiFeBO_3$ $\mathbf{k}$ = (${}^1/_2$, ${}^1/_2$, ${}^1/_2$)				
Fe1a (0.1613, 0.3329, 0.1235)	0	1.73(22)	−2.64(16)	3.16(5)
Fe1b (0.8387, 0.6671, 0.8765)	0	1.73(22)	−2.64(16)	3.16(5)
Fe2a (0.8387, 0.3349, 0.3765)	0	−1.73(22)	2.64(16)	−3.16(5)
Fe2b (0.1613, 0.6671, 0.6235)	0	−1.73(22)	2.64(16)	−3.16(5)
$LiCoBO_3$ $\mathbf{k}$ = (${}^1/_2$, ${}^1/_2$, ${}^1/_2$)				
Co1a (0.1593, 0.3337, 0.1247)	2.85(6)	0	−0.91(6)	3.02(5)
Co1b (0.8407, 0.6663, 0.8753)	2.85(6)	0	−0.91(6)	3.02(5)
Co2a (0.8407, 0.3337, 0.3753)	−2.85(6)	0	0.91(6)	−3.02(5)
Co2b (0.1593, 0.6663, 0.6247)	−2.85(6)	0	0.91(6)	−3.02(5)

3.3.3. Magnetic Structure of $LiFeBO_3$ and $LiCoBO_3$. The magnetic reflections of both $LiFeBO_3$ and $LiCoBO_3$ at $T = 2$ K exist at different scattering vectors and have different intensities than the ones found for M = Mn, indicative of a different magnetic ground state. The $\mathbf{k} = (1, 0, 0)$ propagation vector does not index the observed magnetic peaks, and we found that the smallest propagation vector able to index all of the magnetic reflections is $\mathbf{k} = (^1/_2, ^1/_2, ^1/_2)$, which indicates an 8-fold enlargement of the nuclear unit cell $(2 \times a, 2 \times b, 2 \times c)$. From the loss of the $(\bar{x}, y, \bar{z} + ^1/_2)$ symmetry operation, Fe and Co sites (Wyckoff site 8*f*) split in 2 orbits of multiplicity 4 that we note Fe1 and Fe2, and Co1 and Co2, respectively. In each orbit we label as Fe1a and Fe1b (respectively Co1a and Co1b), the two atoms deduced by the inversion $(\bar{x}, \bar{y}, \bar{z})$. The *C* lattice centering is conserved and generates the other four atoms. For sake of clarity, Table 3 indicates the atomic positions of the atoms carrying a magnetic moment in the cell. With $\mathbf{k} = (^1/_2, ^1/_2, ^1/_2)$, the total magnetic representation Γ can be decomposed on two irreducible representations of dimension 1 as follows

$$\Gamma(8f) = 3\Gamma_1 + 3\Gamma_2$$

which leads to 2 possible spin configurations

$$\Gamma_1:\ F^X = S_a^X + S_b^X \quad F^Y = S_a^Y + S_b^Y \quad F^Z = S_a^Z + S_b^Z$$

$$\Gamma_2:\ A^X = S_a^X - S_b^X \quad A^Y = S_a^Y - S_b^Y \quad A^Z = S_a^Z - S_b^Z$$

where S_a^X and S_b^X are the components along *x* of the magnetic moment of atom *a* and *b* of the same orbit. We tried all the possibilities given by symmetry, with either antiparallel or parallel coupling between the two orbits Fe1 and Fe2 (respectively, Co1 and Co2).

For $LiFeBO_3$, a solution following Γ_2, with an antiparallel coupling between the two orbits, gives the best agreement between observed and calculated patterns (R_{mag} = 4.33%, Figure 7b). The components along **a**, **b**, and **c** were all first refined but as the component along **a** leads to a very small value, it was set to be equal to zero. The magnetic moment on each Fe^{2+} lies therefore within the (**b**, **c**) plane, in the direction the $[02\bar{3}]$, the magnetic structure is collinear (Figure 9b) with a refined value of 3.16(5) μ_B. As shown in Figure 7b, the main magnetic peak at $2\theta = 17.0°$ is severely asymmetric, indicating that even at 2 K the magnetic moments are probably not perfectly ordered. This may be at the origin of the slightly lower magnetic moment value expected for spin-only contributions [4 μ_B ($S = 2$) for a $3d^6$ spin]. However, we cannot rule out the possibility that the electronic configuration has a significant unquenched orbital moment, giving rise to a $J = ^3/_2$ ground state. The fact that the ordered iron moment points primarily along the axial crystal field axis suggests, as in the case of the Mn counterpart, a significant Ising character and unquenched orbital momentum.

For $LiCoBO_3$, the pattern at $T = 2$ K is rather similar, which comes as no surprise considering that the magnetic structure also follows Γ_2, with an antiparallel coupling between the two orbits. Only the direction of the moments is found to be different than for the Fe-based compound. The main magnetic moment is oriented along the *a*-axis. An improvement in the quality of the fit of the magnetic structure is achieved by including a minor component oriented along the *c*-axis (R_{mag} = 10.8% versus 12.5%), leading to moments collinear to the $[30\bar{1}]$ direction. Refining a component along the *b*-axis led to a tiny value without improving the fit, and it was therefore set to zero for the final refinements (Figures 7c and 9c). The refined magnetic moment value of 3.02(5) μ_B is in good agreement with values expected for high spin Co^{2+} $(3d^7, e''^4e'^2a_1'^1)$ in trigonal bipyramid coordination with no orbital contribution. The fully quenched orbital momentum in this environment is suggestive of isotropic, Heisenberg spins.

4. DISCUSSION

From the temperature evolution of the magnetic order parameter (refined magnetic moment), we determined the Néel temperature T_{N2}, indicative of the inset of the ground state magnetic ordering (Figure 8). The higher Néel temperatures for Fe ($T_{N2} \sim 25(1)$ K) compared to Co and Mn [$T_{N2} \sim 12(1)$ K for $LiCoBO_3$ and $T_{N2} \sim 12(1)$ K for $LiMnBO_3$] are similar to the trends observed with $(Na/Li)MSO_4F$.[15,16]

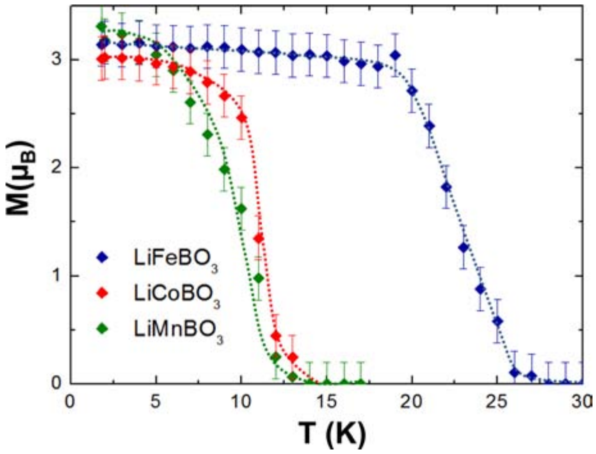

Figure 8. Temperature dependence of the ordered magnetic moment in the long-range ordered magnetic structure. The dotted lines are guide for the eyes.

Figure 9 illustrates the magnetic structures for each compound. For $LiFeBO_3$ and $LiCoBO_3$, neighboring Fe^{2+}/Co^{2+} moments in the edge-sharing MO_5 trigonal bipyramids ribbons are parallel. These ferromagnetic chains are coupled

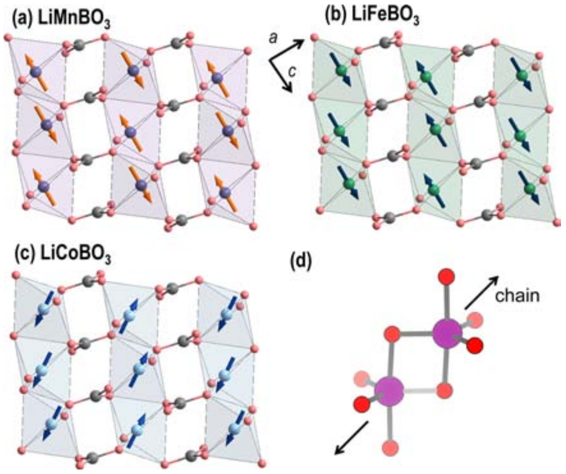

Figure 9. Illustration of the magnetic structures for (a) $LiMnBO_3$, (b) $LiFeBO_3$, and (c) $LiCoBO_3$. The magnetic moment orientations on the Fe^{2+}, Co^{2+}, and Mn^{2+} ions are indicated with arrows. (d) Super exchange path occurring when two MO_5 trigonal bipyramids are linked through an edge.

antiferromagnetically so that the resulting behavior is antiferromagnetic. From the iron to the cobalt counterparts, magnetic moments turn from the $[02\bar{3}]$ direction to the $[30\bar{1}]$ direction. The ground state for $LiMnBO_3$ is completely different, as neighboring Mn^{2+} spins within the chains are antiferromagnetically coupled with a moment ~3.31 μ_B along the *c*-axis. Our results for $LiMnBO_3$ are in agreement with Zhao et al.'s predictions.[37] Interestingly, the magnetic moment of Mn points from one apex to another within the trigonal bipyramid, whereas the $[30\bar{1}]$ direction of the Co magnetic moments corresponds to a direction almost perfectly in the basal plane. At the opposite, the $[02\bar{3}]$ direction for iron moments seems random regarding the local coordination. The orientation of the moment direction along specific crystal field axes for $LiMnBO_3$ suggests unquenched orbital momentum; this imparts an Ising character to the magnetic spins and suggests that interesting physics or excitations may persist from competing interactions between the single-ion anisotropy and external magnetic fields.

In polyanionic structures, the driving force to establish a magnetic long-range ordering lays in the super and super-super exchange interactions as developed by Goodenough in the late 1950s on perovskites.[38] The sign and strength of this exchange depend on two main factors: (1) the geometrical characteristics (bond length and angles) of the M−O−M or M−O−O−M paths for super and super-super exchange, respectively, and (2) the distribution of electrons on orbitals. If these interactions have been widely studied for transition metals sitting on octahedral environments, much less work was devoted to less usual coordinations such as trigonal bipyramids. This kind of coordination was previously encountered in $LuFe_2O_4$ but was in competition with a direct M−M interaction, and the resulting magnetic structures are extremely complex.[39] It was also reported in the $Li_2FeP_2O_7$ pyrophosphate, whose adjacent FeO_5 bipyramids are ferromagnetically coupled,[14] as in the present case. Orthoferrite compounds and their Mn equivalent $YMnO_3$ and $ScMnO_3$ also present trigonal bipyramids MnO_5, but the arrangement is totally different from our case as they form layers.[40] Looking back to the topology, the $LiMBO_3$ system presents two kinds of interactions: a double superexchange path along the chains, linking adjacent M atoms, and super-super exchange interactions that couple M atoms from one chain to another, via two oxygen atoms belonging to a BO_3 triangle. The complexity of the structure is such that each BO_3 links three different chains, so there is difficulty to simplify easily the system with one single intrachain interaction. Looking into the super exchange along one single chain (Figure 9d), we can notice that in all three compounds distances and M−O−M angles are similar (ranging from 92° to 96°). Therefore, this geometric argument cannot explain why this interaction is antiferromagnetic for Mn and ferromagnetic for Co and Fe. The origin of such behavior should rather depend on the electron distribution in the five d orbitals in trigonal bipyramid environment and the way they overlap with 2p orbitals from oxygen. Obviously, this addresses new questions to theorists, and we believe that $LiMBO_3$ systems may serve as model compounds.

5. CONCLUSION

The magnetic behavior of $LiMBO_3$ (M = Mn, Fe, Co) compounds has been studied from temperature dependent susceptibility measurements, and the magnetic structures have been solved from neutron powder diffraction data. Each compound undergoes two successive magnetic ordering transitions, from a paramagnetic state to an incommensurately ordered magnetic state followed by a long-range ordered commensurate antiferromagnetic ground state at lower temperature. The magnetic structures at $T = 2$ K consist of ferromagnetic Ising chains with antiferromagnetic interactions between each chain for $LiFeBO_3$ and a ferromagnetic Heisenberg chain with antiferromagnetic interactions between each chain for $LiCoBO_3$. The manganese analogue presents antiferromagnetic edge-sharing MnO_5 chains coupled antiferromagnetically. The most remarkable feature of the magnetic behavior of these compounds arises from the trigonal bipyrimidal coordination of the metal center: $LiCoBO_3$ is an uncommon example of a cobalt-containing compound without strong Ising character, and there are unusually large unquenched orbital angular momenta in the Mn^{2+} (d^5) and Fe^{2+} (d^6) analogues. These results confirm that unique coordination environments can give rise to novel electronic and magnetic phenomena, and the preparation of other related compounds should derive further interest.

■ ASSOCIATED CONTENT

Ⓢ Supporting Information

Evolution of the unit cell volume and cell parameters versus temperature, deduced from neutron powder diffraction, for $LiMnBO_3$, $LiFeBO_3$, and $LiCoBO_3$. This material is available free of charge via the Internet at http://pubs.acs.org.

■ AUTHOR INFORMATION

Corresponding Author

*E-mail: gwenaelle.rousse@upmc.fr.

Present Address

$^{\perp}$Department of Chemistry, Colorado State University, Fort Collins, CO 80524.

Notes

The authors declare no competing financial interest.

■ ACKNOWLEDGMENTS

We acknowledge the Centre National de la Recherche Scientifique (CNRS) and UMICORE (Belgium) for the Ph.D. Grant of L.T. The authors thank Thomas C. Hansen, Jean-Noël Chotard, and Marine Reynaud for help with collection of neutron diffraction data and ILL for awarding beamtime. G.R. thanks Juan Rodríguez-Carvajal and Guillaume Radtke for fruitful discussions. J.R.N. and T.M.M. acknowledge support from startup funds from the Johns Hopkins University, and the David and Lucile Packard Foundation.

■ REFERENCES

(1) Padhi, A. K.; Nanjundaswamy, K. S.; Masquelier, C.; Okada, S.; Goodenough, J. B. *J. Electrochem. Soc.* **1997**, *144* (5), 1609−1613.

(2) Padhi, A. K.; Nanjundaswamy, K. S.; Goodenough, J. B. *J. Electrochem. Soc.* **1997**, *144* (4), 1188−1194.

(3) Nishimura, S.-i.; Hayase, S.; Kanno, R.; Yashima, M.; Nakayama, N.; Yamada, A. *J. Am. Chem. Soc.* **2008**, *130* (40), 13212−13213.

(4) Sirisopanaporn, C.; Masquelier, C.; Bruce, P. G.; Armstrong, A. R.; Dominko, R. *J. Am. Chem. Soc.* **2010**, *133* (5), 1263−1265.

(5) Islam, M. S.; Dominko, R.; Masquelier, C.; Sirisopanaporn, C.; Armstrong, A. R.; Bruce, P. G. *J. Mater. Chem.* **2011**, *21* (27), 9811−9818.

(6) Legagneur, V.; An, Y.; Mosbah, A.; Portal, R.; Le Gal La Salle, A.; Verbaere, A.; Guyomard, D.; Piffard, Y. *Solid State Ionics* **2001**, *139* (1−2), 37−46.

(7) Yamada, A.; Iwane, N.; Harada, Y.; Nishimura, S.-i.; Koyama, Y.; Tanaka, I. *Adv. Mater.* **2010**, *22* (32), 3583−3587.

(8) Recham, N.; Chotard, J. N.; Dupont, L.; Delacourt, C.; Walker, W.; Armand, M.; Tarascon, J. M. *Nat. Mater.* **2010**, *9* (1), 68−74.

(9) Tripathi, R.; Ramesh, T. N.; Ellis, B. L.; Nazar, L. F. *Angew. Chem., Int. Ed.* **2010**, *49* (46), 8738−8742.
(10) Barpanda, P.; Ati, M.; Melot, B. C.; Rousse, G.; Chotard, J. N.; Doublet, M. L.; Sougrati, M. T.; Corr, S. A.; Jumas, J. C.; Tarascon, J. M. *Nat. Mater.* **2011**, *10* (10), 772−779.
(11) Rousse, G.; Rodriguez-Carvajal, J.; Wurm, C.; Masquelier, C. *Chem. Mater.* **2001**, *13* (12), 4527−4536.
(12) Rousse, G.; Rodriguez-Carvajal, J.; Patoux, S.; Masquelier, C. *Chem. Mater.* **2003**, *15* (21), 4082−4090.
(13) Rousse, G.; Rodriguez-Carvajal, J.; Wurm, C.; Masquelier, C. *Solid State Sci.* **2002**, *4* (7), 973−978.
(14) Barpanda, P.; Rousse, G.; Ye, T.; Ling, C. D.; Mohamed, Z.; Klein, Y.; Yamada, A. *Inorg. Chem.* **2013**, *52* (6), 3334−3341.
(15) Melot, B. C.; Rousse, G.; Chotard, J. N.; Ati, M.; Rodríguez-Carvajal, J.; Kemei, M. C.; Tarascon, J. M. *Chem. Mater.* **2011**, *23* (11), 2922−2930.
(16) Melot, B. C.; Rousse, G.; Chotard, J. N.; Kemei, M. C.; Rodríguez-Carvajal, J.; Tarascon, J. M. *Phys. Rev. B* **2012**, *85* (9), 094415.
(17) Dong, Y. Z.; Zhao, Y. M.; Shi, Z. D.; An, X. N.; Fu, P.; Chen, L. *Electrochim. Acta* **2008**, *53* (5), 2339−2345.
(18) Chen, L.; Zhao, Y.; An, X.; Liu, J.; Dong, Y.; Chen, Y.; Kuang, Q. *J. Alloys Compd.* **2010**, *494* (1−2), 415−419.
(19) Kim, J. C.; Moore, C. J.; Kang, B.; Hautier, G.; Jain, A.; Ceder, G. *J. Electrochem. Soc.* **2011**, *158* (3), A309−A315.
(20) Yamada, A.; Iwane, N.; Nishimura, S.-i.; Koyama, Y.; Tanaka, I. *J. Mater. Chem.* **2011**, *21* (29), 10690−10696.
(21) Bo, S.-H.; Wang, F.; Janssen, Y.; Zeng, D.; Nam, K.-W.; Xu, W.; Du, L.-S.; Graetz, J.; Yang, X.-Q.; Zhu, Y.; Parise, J. B.; Grey, C. P.; Khalifah, P. G. *J. Mater. Chem.* **2012**, *22* (18), 8799−8809.
(22) Janssen, Y.; Middlemiss, D. S.; Bo, S.-H.; Grey, C. P.; Khalifah, P. G. *J. Am. Chem. Soc.* **2012**, *134* (30), 12516−12527.
(23) Dutton, S. E.; Kumar, M.; Mourigal, M.; Soos, Z. G.; Wen, J. J.; Broholm, C. L.; Andersen, N. H.; Huang, Q.; Zbiri, M.; Toft-Petersen, R.; Cava, R. J. *Phys. Rev. Lett.* **2012**, *108* (18), 187206.
(24) Melot, B. C.; Goldman, A.; Darago, L. E.; Furman, J. D.; Rodriguez, E. E.; Seshadri, R. *J. Phys.: Condens. Matter* **2010**, *22* (50), 506003.
(25) Tao, L.; Rousse, G.; Chotard, J. N.; Dupont, L.; Bruyère, S.; Hanzel, D.; Mali, G.; Dominko, R.; Levasseur, S.; Masquelier, C. Preparation, Structure and Electrochemistry of $LiFeBO_3$: a Cathode Material for Li-ion Battery. Submitted, **2013.**
(26) Neilson, J. R.; McQueen, T. M.; Llobet, A.; Wen, J.; Suchomel, M. R. *Phys. Rev. B* **2013**, *87* (4), 045124.
(27) Denis Romero, F.; Burr, S. J.; McGrady, J. E.; Gianolio, D.; Cibin, G.; Hayward, M. A. *J. Am. Chem. Soc.* **2013**, *135* (5), 1838−1844.
(28) Rietveld, H. M. *J. Appl. Crystallogr.* **1969**, *2*, 65.
(29) Rodriguez-Carvajal, J. *Phys. B* **1993**, *192*, 55.
(30) Bertaut, E. F. *J. Phys., Colloq.* **1971**, *C1*, 32.
(31) Brown, I. D.; Shannon, R. D. *Acta Crystallogr.* **1973**, *A26*, 266.
(32) Li, R. K.; Chen, C. T.; Greaves, C. *Phys. Rev. B* **2002**, *66* (5), 052405.
(33) McQueen, T.; Huang, Q.; Lynn, J. W.; Berger, R. F.; Klimczuk, T.; Ueland, B. G.; Schiffer, P.; Cava, R. J. *Phys. Rev. B* **2007**, *76* (2), 024420.
(34) Lorenz, W. E. A.; Kuzian, R. O.; Drechsler, S.-L.; Stein, W.-D.; Wizent, N.; Behr, G.; Málek, J.; Nitzsche, U.; Rosner, H.; Hiess, A.; Schmidt, W.; Klingeler, R.; Loewenhaupt, M.; Büchner, B. *Europhys. Lett.* **2009**, *88* (3), 37002.
(35) Capogna, L.; Mayr, M.; Horsch, P.; Raichle, M.; Kremer, R. K.; Sofin, M.; Maljuk, A.; Jansen, M.; Keimer, B. *Phys. Rev. B* **2005**, *71* (14), 140402.
(36) Mourigal, M.; Enderle, M.; Kremer, R. K.; Law, J. M.; Fåk, B. *Phys. Rev. B* **2011**, *83* (10), 100409.
(37) Lin, Z.; Zhao, Y.-J.; Zhao, Y. *Phys. Lett. A* **2012**, *376* (3), 179−184.
(38) Goodenough, J. B. *J. Phys. Chem. Solids* **1958**, *6* (2−3), 287−297.
(39) Bourgeois, J.; Andre, G.; Petit, S.; Robert, J.; Poienar, M.; Rouquette, J.; Elkaim, E.; Hervieu, M.; Maignan, A.; Martin, C.; Damay, F. *Phys. Rev. B* **2012**, *86*, (2).
(40) Munoz, A.; Alonso, J. A.; Martinez-Lope, M. J.; Casais, M. T.; Martinez, J. L.; Fernandez-Diaz, M. T. *Phys. Rev. B* **2000**, *62* (14), 9498−9510.